



# Homogeneous ignition of $\text{H}_2/\text{CO}/\text{O}_2/\text{N}_2$ mixtures over palladium at pressures up to 8 bar<sup>☆</sup>

Ran Sui<sup>a,b</sup>, John Mantzaras<sup>a,\*</sup>, Chung K. Law<sup>b</sup>, Rolf Bombach<sup>c</sup>,  
Meysam Khatoonabadi<sup>a</sup>

<sup>a</sup> Paul Scherrer Institute, Laboratory for Scientific Computing and Modeling, CH-5232 Villigen PSI, Switzerland

<sup>b</sup> Princeton University, Department of Mechanical and Aerospace Engineering, Princeton, NJ 08544, United States

<sup>c</sup> Paul Scherrer Institute, Energy System Integration Platform, CH-5232 Villigen PSI, Switzerland

Received 6 November 2019; accepted 11 June 2020

Available online xxx

## Abstract

The catalytic and gas-phase combustion of fuel-lean  $\text{H}_2/\text{CO}/\text{O}_2/\text{N}_2$  mixtures over palladium was investigated experimentally and numerically at a global equivalence ratio  $\varphi = 0.285$ ,  $\text{H}_2/\text{CO}$  volumetric ratios 1–4, pressures 1–8 bar and catalyst surface temperatures 950–1200 K. In situ planar laser induced fluorescence (PLIF) of the OH radical monitored homogeneous combustion inside a channel-flow catalytic reactor, while 1-D Raman measurements of main gas-phase species concentrations across the channel boundary layer assessed the heterogeneous processes. Simulations were carried out with a 2-D numerical code using detailed heterogeneous and homogeneous chemical reaction mechanisms and realistic transport. The simulated and measured transverse species profiles attested to a transport-limited catalytic conversion of  $\text{H}_2$  and CO at all operating conditions. The OH-PLIF measurements and the simulations confirmed the establishment of appreciable homogeneous combustion only for  $p < 4$  bar, with progressively diminishing gas-phase contribution as the pressure increased from 4 to 8 bar. This strong pressure dependence reflected the complex pressure/temperature dependence of the homogeneous ignition chemistry as well as the competition between the catalytic and gaseous reaction pathways for  $\text{H}_2$  and CO consumption. Over the gaseous induction zones ( $x < x_{\text{ig}}$ ), the wall temperatures were below the pressure-dependent upper temperature limit for the decomposition of PdO to metallic Pd. Even though palladium catalysts exhibited a “self-regulating” temperature effect due to the decomposition of PdO, the attained temperatures were still sufficient to ignite homogeneous combustion of the  $\text{H}_2/\text{CO}/\text{O}_2/\text{N}_2$  mixtures, in contrast to hydrocarbon fuels for which gas-phase combustion was largely suppressed over PdO in the pressure range 1–8 bar. The results indicated that for the elevated

<sup>☆</sup> Submission to the Proceedings of the Combustion Institute, 38th International Symposium on Combustion, January 24–29, Adelaide, Australia

\* Corresponding author.

E-mail address: [ioannis.mantzaras@psi.ch](mailto:ioannis.mantzaras@psi.ch) (J. Mantzaras).

<https://doi.org/10.1016/j.proci.2020.06.262>

1540-7489 © 2020 The Combustion Institute. Published by Elsevier Inc. All rights reserved.

pressures and preheats of syngas-fueled hetero-/homogeneous combustion power systems, gas-phase chemistry cannot be ignored during reactor design.

© 2020 The Combustion Institute. Published by Elsevier Inc. All rights reserved.

**Keywords:** Syngas combustion over palladium; In situ Raman and OH-PLIF measurements; Homogeneous ignition of syngas over palladium at elevated pressures; Self-regulating temperature of palladium

## 1. Introduction

Combustion of environmentally-friendly syngas and biogas fuels is of primary interest in large-scale power generation. Integrated Gasification Combined Cycle (IGCC) concepts [1] utilize pre-combustion CO<sub>2</sub> capture by gasifying liquid and solid fossil fuels and transforming them to syngas, a gas that largely comprises CO and H<sub>2</sub>. The H<sub>2</sub>:CO volumetric ratio can be further adjusted by adding a Water Gas Shift (WGS) reactor downstream of the gasifier. In addition to solid and liquid fuels, pre-combustion CO<sub>2</sub> capture is pursued in natural-gas-fueled turbines by reforming the natural gas to syngas [2]. Syngas or biogas fuels with small CO<sub>2</sub> footprint are also appealing for micro-scale power generation [3,4].

Combined heterogeneous (catalytic) and homogeneous (gas-phase) combustion methods have been investigated for large-scale power generation with syngas fuels [5–7]. This is because the standard lean-premixed homogeneous combustion of high-hydrogen-content fuels is susceptible to flashback, while hetero-/homogeneous combustion diminishes this hazard due to the inhibiting effect of catalytic reactions on upstream flame propagation [8]. Moreover, hybrid hetero-/homogeneous combustion methods substantially reduce the NO<sub>x</sub> emissions compared to conventional gas-phase combustion [9].

The catalytic combustion of H<sub>2</sub>/CO blends over Pt, Rh and Pd noble metals has been studied at modest temperatures 500–800 K [10–14], revealing complex chemical interactions whereby one fuel component may inhibit the oxidation of the other [12–14]. Palladium is the most active catalyst for the complete oxidation of methane at temperatures up to 900 K and, for fuel flexibility, is the preferred catalyst for power systems operating either with natural gas or syngas. At ambient oxygen partial pressure the active PdO phase decomposes above ~1070 K to the less active metallic Pd phase, which re-oxidizes to PdO below ~870 K thus creating a hysteresis in the fuel conversion during heating/cooling cycles [15]. The PdO decomposition temperature depends on the catalyst support and catalyst particle size [16] and increases with increasing oxygen partial pressure [17,18]. While light-off studies of H<sub>2</sub>, CO and H<sub>2</sub>/CO mixtures over PdO have been performed at temperatures up

to 750 K [14,18], in steady operation of power generation systems the catalyst temperatures typically exceed 950 K [7,19]. At such high temperatures and for the elevated pressures of power generation systems, it has been shown that gas-phase combustion can be ignited over Pt and Rh catalysts when using hydrocarbon or syngas fuels [5,20–22]. However, Pd catalysts “self-regulate” their surface temperatures [19] due to the decomposition of the active PdO phase to Pd, which can in turn suppress the onset of homogeneous ignition. In a recent study [23], we reported that gaseous combustion is largely inhibited during the high-pressure combustion of CH<sub>4</sub> over PdO.

The understanding of hetero-/homogeneous combustion has been fostered by non-intrusive Raman measurements of major species concentrations and planar laser induced fluorescence (PLIF) of radical species [24], while the applicability of major species PLIF (O<sub>2</sub>, CO<sub>2</sub>) over catalytic surfaces has been demonstrated recently [25,26]. The present work investigates the combustion of fuel-lean H<sub>2</sub>/CO/O<sub>2</sub>/N<sub>2</sub> mixtures over palladium at pressures of 1–8 bar (of interest to microreactors and small-scale gas turbines), surface temperatures of 950–1200 K (typical to deep oxidation temperatures in power generation systems), and H<sub>2</sub>:CO volumetric ratios of 1 to 4. In situ 1-D Raman measurements of the major gas-phase species concentrations and OH-PLIF monitored the catalytic and gas-phase processes, respectively. 2-D simulations were carried out with detailed hetero-/homogeneous chemistry, in order to validate the employed chemical reaction mechanisms by comparing the predictions with the measurements. The main objective was to examine the potential of homogeneous combustion and its dependence on pressure, temperature and H<sub>2</sub>:CO volumetric ratio.

## 2. Experimental

### 2.1. High-pressure reactor

A channel-flow catalytic reactor was affixed inside a high-pressure cylindrical tank (Fig. 1 and [13,27]). The reactor was made of two 9-mm-thick horizontal Si[SiC] ceramic plates, 300 mm long (-x), 104 mm wide (-z), positioned 7 mm apart (-y), and two 3-mm-thick vertical quartz windows (Fig. 1a). Using Plasma Vapor Deposition (PVD),

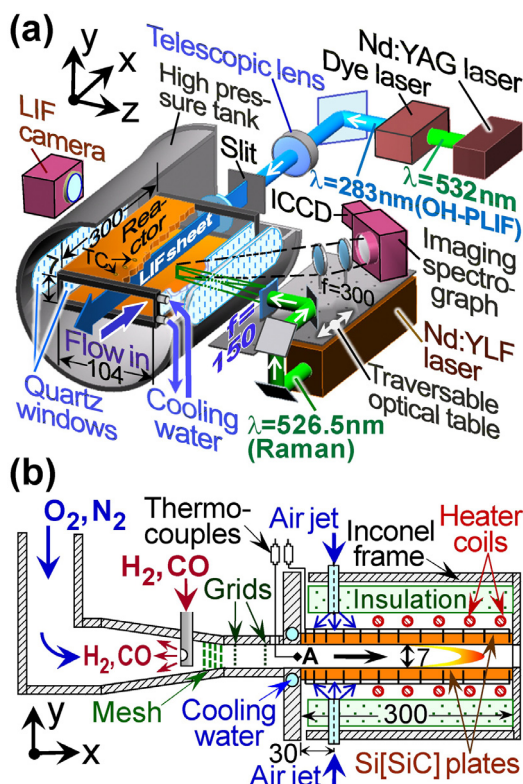


Fig. 1. (a) Raman/O-H-PLIF optical setups and test-rig, (b) reactor details (dimensions in mm).

the inner Si[SiC] surfaces were first coated with a 1.5  $\mu\text{m}$  thick non-porous  $\text{Al}_2\text{O}_3$  layer and subsequently with a 2.2  $\mu\text{m}$  thick Pd layer. The appreciably thick Pd layer resembled a polycrystalline surface, as reported in earlier studies [23]. Furthermore, X-ray photoelectron spectroscopy (XPS) attested to the absence of Al or Si from the catalyst surface. Surface temperatures along the  $x$ - $y$  symmetry plane were measured with 12 S-type thermocouples (on each plate), embedded 0.9 mm below the catalyst through 8.1-mm-deep holes eroded from the outside Si[SiC] surfaces. Optical accessibility from both reactor sides was accomplished by two 350-mm-long and 35-mm-thick quartz windows on the high-pressure tank (Fig. 1a). Two additional windows, one at the rear tank flange and the other at the reactor exhaust (Fig. 1a), yielded a counterflow optical access for the OH-PLIF experiments.

The sub-unity Lewis number of the  $\text{H}_2$  component ( $Le_{\text{H}_2} \sim 0.3$  at fuel-lean stoichiometries in air) produced superadiabatic catalyst surface temperatures [24,27]. To suppress this detrimental (for the catalyst/reactor integrity) superadiabaticity and at the same time stabilize combustion, a heating/cooling arrangement was adopted [5,28]. The

front faces of the Si[SiC] plates ( $104 \times 7 \text{ mm}^2$ ) contacted a water-cooled section of an Inconel support frame (Fig. 1), while the Si[SiC] rear parts  $100 < x < 300 \text{ mm}$  ( $x = 0$  denotes the catalyst start) were mildly heated by two adjustable-power resistive coils to counteract conduction heat losses to the Inconel frame that may have extinguished combustion. For finer temperature control, two adjustable-flow cooling air-jets issuing from two rectangular slots ( $10 \times 100 \text{ mm}^2$  in  $x$ - $z$ , located at  $x = 30 \text{ mm}$ ) impinged on the outer Si[SiC] surfaces (Fig. 1b).

Batteries supplied gases and four Brooks mass flow meters regulated the  $\text{O}_2/\text{N}_2/\text{CO}/\text{H}_2$  flows. Two streams of  $\text{O}_2/\text{N}_2$  and  $\text{H}_2/\text{CO}$  (99.95% purity) were formed and mixed in a 200-mm-long steel conical section (Fig. 1b), having an ending cross-flow area equal to that of the channel reactor ( $104 \times 7 \text{ mm}^2$ ). A wire mesh and two fine grids produced uniform exit velocity and good mixing of the  $\text{H}_2/\text{CO}$  and  $\text{O}_2/\text{N}_2$  streams. At the exit of the conical section, hot wire velocimetry assessed the flow uniformity while NO-PLIF (100 ppmv NO doped into  $\text{H}_2/\text{CO}$ , excitation at 226.25 nm and detection at 240–265 nm) established the good mixing quality. A sheathed thermocouple at the channel entry (location “A” in Fig. 1b) recorded the gas inlet temperature.

## 2.2. Laser diagnostics

The Raman/OH-PLIF setups are illustrated in Fig. 1a. Raman excitation was provided by a frequency-doubled pulsed Nd:YLF laser (Quantronix Darwin-Duo, 526.5 nm, repetition frequency 2 kHz, 120 ns pulse duration, 40 mJ pulse energy). An  $f = 150 \text{ mm}$  cylindrical lens focused the beam into a  $\sim 0.3 \text{ mm}$  thick vertical line, which spanned the 7 mm channel height and was offset laterally ( $z = 15 \text{ mm}$ ) to increase the light collection angle and diminish thermal beam steering [21,23]. Two  $f = 300 \text{ mm}$  spherical lenses focused the Raman-scattered light into the entry slit of a 25 cm spectrograph (Chromex-250i,  $f/4.0$ ) that had an intensified CCD-camera (Princeton Instruments PI-MAX1024GIII) with  $640 \times 255$  pixels corresponding to spectral shift and channel height, respectively; the 255-pixel height was further binned to 64 pixels. An OG550 Schott colored glass and a tilted 532 nm holographic notch filter (Kaiser-Optical Systems) suppressed the excitation radiation. The laser, spectrograph and all optical components were mounted on a traversable optical table (Fig. 1a), permitting measurements over  $8 \leq x \leq 126 \text{ mm}$ . Given the steady operating conditions, scattered light from 240,000–300,000 laser pulses was collected on the detector to improve the signal-to-noise ratio. Effective Raman cross-sections, including transmission efficiencies, were assessed by recording signals of pressurized air,  $\text{N}_2$ , and the actual reactive mixtures [22].

Measurement accuracy was  $\pm 4\%$  for species volumetric contents  $\geq 3\%$  and  $\pm 8\%$  for contents down to  $0.5\%$ , whereas lower compositions could not be accurately detected. Measurements within  $0.5\text{--}0.7\text{ mm}$  from either wall were discarded because of low signal-to-noise ratios.

The OH-PLIF employed a frequency-doubled pulsed Nd:YAG laser (Quantel YG781C20 CL-D-LNE3,  $532\text{ nm}$ ,  $10\text{ ns}$  pulse duration,  $20\text{ Hz}$  repetition rate), which pumped a Quantel TDL90-NBP2EWT UVT3 dye laser. The dye radiation was frequency-doubled at  $283.3\text{ nm}$  to excite the A-X(1,0)  $Q_1(7)$  OH transition. The excitation beam was transformed by a telescopic lens and a slit-mask into a vertical light-sheet propagating counterflow along the  $x$ - $y$  symmetry plane (Fig. 1a). Fluorescence was collected at  $90^\circ$  through the reactor and tank side windows and recorded by an intensified CCD camera (LaVision-Imager-Compact HiRes-IRO,  $1392 \times 1024$  pixels). Fluorescence from both (1-1) and (0-0) transitions at  $308$  and  $314\text{ nm}$ , respectively, was collected by a Coastal-Optics UV Nikkor  $f=100/4.5$  lens equipped with a bk310-11-C interference filter. Up to  $800$  pulses were integrated on  $1360 \times 120$  pixels of the CCD chip, corresponding to  $100 \times 7\text{ mm}^2$  ( $x$ - $y$ ) area.

### 3. Numerical

A steady Navier-Stokes 2-D CFD code [13,27] with a staggered grid of  $480 \times 124$  points (in  $x$ - $y$ , for the  $300 \times 7\text{ mm}^2$  domain) yielded grid-independent solutions. At the inlet, the axial velocity, species mass fractions and temperature were uniform. Curves fitted through the 12 thermocouple measurements provided temperature profiles for the lower ( $y=0$ ) and upper ( $y=7\text{ mm}$ ) channel walls that were imposed as boundary conditions.

The  $\text{H}_2/\text{CO}$  subset of the methane catalytic mechanism over PdO from Shimizu and Wang [29] was used (21 reactions, 6 surface and 8 gaseous species, surface site density  $1.95 \times 10^{-9}\text{ mol/cm}^2$ , see Table S1), which has been validated for PdO and Pd at  $300\text{--}1500\text{ K}$  (thus encompassing the surface temperatures of the present study). The mechanism was developed for PdO/Pd nanoparticles, however, in a more recent study Wang and Law et al. [30] published a mechanism for  $\text{CH}_4$  oxidation on bulk PdO/Pd wires rather than on nanoparticles. The two mechanisms had the same basic kinetic parameters for the  $\text{H}_2/\text{CO}$  subset. Furthermore, it was shown [30] that with a fully oxidized surface, the PdO layer was  $1\text{--}2\text{ }\mu\text{m}$  thick, which should exclude strong Pd-support interactions. Therefore, our fully pre-oxidized catalyst should perform the same as PdO nanoparticles. Finally, the precise surface kinetics do not control homogeneous ignition since, as will be shown next, the catalytic conversion of

Table 1  
Experimental conditions<sup>a</sup>.

Case	$p$	$U_{\text{IN}}$	$\text{H}_2$	$\text{H}_2:\text{CO}$
(A1, B1, C1)	1.0	5.8	(8.2, 7.5, 6.7)	(4, 2, 1)
(A2, B2, C2)	1.5	3.9	(8.2, 7.5, 6.7)	(4, 2, 1)
(A3, B3, C3)	2.5	2.4	(8.2, 7.5, 6.7)	(4, 2, 1)
(A4, B4, C4)	4.0	1.5	(8.2, 7.5, 6.7)	(4, 2, 1)
(A5, B5, C5)	6.0	1.0	(8.2, 7.5, 6.7)	(4, 2, 1)
(A6, B6, C6)	8.0	0.7	(8.2, 7.5, 6.7)	(4, 2, 1)

<sup>a</sup> Pressure (bar), inlet velocity (m/s),  $\text{H}_2$  volumetric content (%),  $\text{H}_2:\text{CO}$  volumetric ratio.

both CO and  $\text{H}_2$  is transport controlled and not kinetically controlled.

For gaseous chemistry, the  $\text{H}_2/\text{O}_2$  mechanism by Burke et al. [31] was coupled to the CO/ $\text{O}_2$  reaction mechanism from Li et al. [32], yielding a mechanism with 36 reversible reactions among 13 species (Table S2). This gaseous mechanism captured homogeneous ignition of fuel-lean  $\text{H}_2/\text{CO}/\text{air}$  mixtures over Pt in [33]. Surface and gaseous reaction rates were calculated with Surface-CHEMKIN [34] and CHEMKIN [35], respectively. A mixture-average diffusion model, including thermal diffusion for H and  $\text{H}_2$  was adopted, using the CHEMKIN transport database [36].

### 4. Results and discussion

Steady combustion of  $\text{H}_2/\text{CO}/\text{O}_2/\text{N}_2$  mixtures was investigated (see Table 1) at a constant global ( $\text{H}_2+\text{CO})/\text{O}_2$  equivalence ratio  $\varphi=0.285$ , pressures  $1\text{--}8\text{ bar}$  and  $\text{H}_2:\text{CO}$  volumetric ratios of 4 (Cases A1–A6), 2 (Cases B1–B6) and 1 (Cases C1–C6). The inlet temperatures were practically the same in all cases ( $T_{\text{IN}}=303\text{--}306\text{ K}$ ), while for a given pressure the inlet velocities ( $U_{\text{IN}}$ ) were constant. Laminar flows were established, with Reynolds numbers up to  $\sim 2250$  based on the inlet properties and the channel height; it is noted that the strong heat transfer from the hot catalytic walls guaranteed laminar flows even at inlet Reynolds numbers up to  $\sim 5000$  [37].

Measured and predicted OH distributions are depicted in Fig. 2. The measurements were produced by overlapping successive  $100\text{-mm}$ -long PLIF images. For those cases where strong flames were established, two separate flame branches running parallel to the catalytic walls were formed, a result of the diffusional imbalance of  $\text{H}_2$  [33]. Asymmetries in the flame shapes were evident in Fig. 2 due to modest temperature differences (up to  $28\text{ K}$ ) between the upper and lower walls, as seen by the wall temperature ( $T_{\text{wall}}$ ) profiles for 9 selected cases in Fig. 3 (temperature profiles for the remaining cases are included in Table S3). The computed adiabatic equilibrium temperatures based on the inlet conditions were  $T_{\text{ad}}=1138\text{ K}$  (Cases A1–A6),  $1231\text{ K}$  (Cases B1–B6) and  $1409\text{ K}$  (Cases



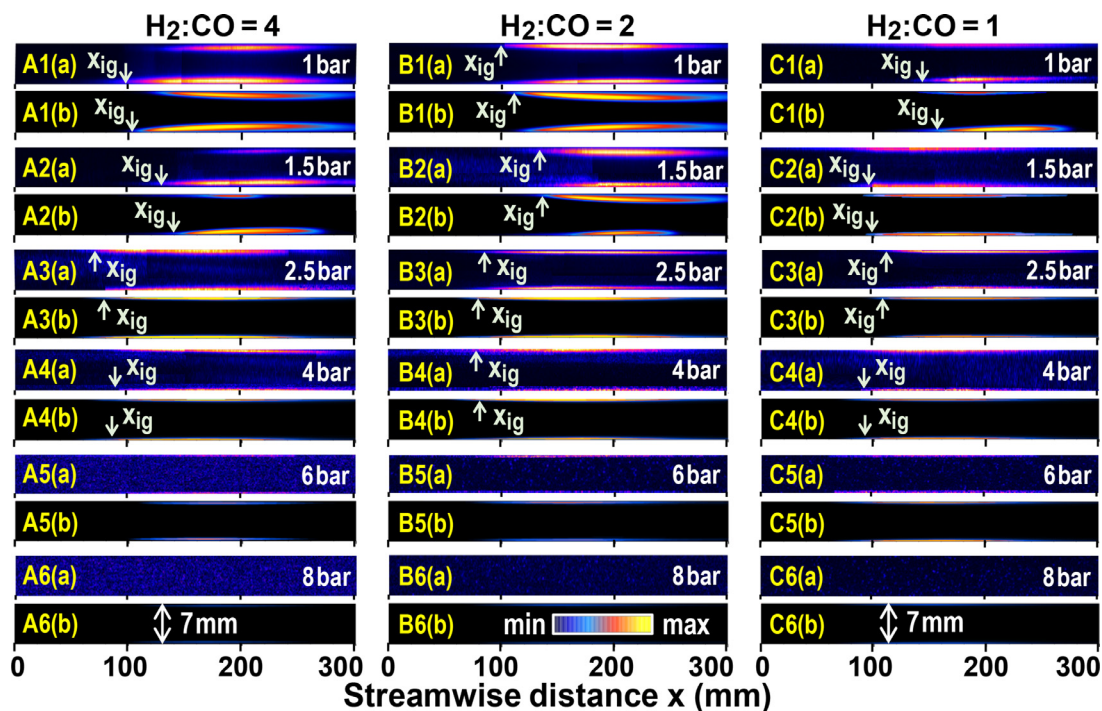


Fig. 2. (a) PLIF-measured and (b) computed OH distributions for all cases. Arrows marked  $x_{ig}$  denote homogeneous ignition positions. Color bar gives the computed OH (minimum = 0 and maximum = 550.2, 282.5, 11.6, 2.7, 0.5, 0.3 ppmv for Cases A1-A6, 596.1, 363.4, 10.3, 2.6, 0.5, 0.2 ppmv for Cases B1-B6 and 286.2, 10.3, 2.6, 1.7, 0.8, 0.2 ppmv for Cases C1-C6).

C1-C6), indicating suppression of the surface superadiabaticity except for Cases A1-A6 where the peak  $T_{wall}$  exceeded modestly  $T_{ad}$  (by 18-72 K). The homogeneous ignition positions ( $x_{ig}$ , marked by arrows in Fig. 2 for those cases where an appreciable homogeneous combustion could be detected), were determined in both measurements and predictions as the far-upstream axial positions whereby OH attained 5% of its maximum value. Over the gas-phase induction zones ( $x < x_{ig}$ ) the wall temperatures were  $950 \text{ K} < T_{wall} < 1196 \text{ K}$ . Differences between predicted and measured  $x_{ig}$  for the cases up to 4 bar, wherein a detectable gaseous combustion was obtained, were 1.2-10.1%.

While the catalyst phase(s) could not be assessed operando and the wall temperatures in Fig. 3 were in some cases high enough to cause PdO decomposition, this was not of concern since the employed catalytic mechanism was valid for both PdO and Pd. However, it was ensured that before the start of each test the catalyst comprised of PdO phase. This was verified by ex-situ X-ray Photoelectron Spectroscopy (XPS) on room-temperature fresh samples and on heated samples (placed 1 hr in an oven with atmospheric-pressure air); sample sizes were  $10 \times 10 \text{ mm}^2$  and were coated with the same procedure as the Si[SiC] plates. After heating, the sam-

ples were cooled to room temperature and analyzed. The XPS spectra in Fig. S1 indicated metallic Pd for the fresh sample and PdO for samples heated to 950-1200 K.

#### 4.1. Hetero-/homogeneous combustion

Axial profiles of computed catalytic (C) and gaseous (G) conversion rates of  $\text{H}_2$  and CO are shown in Fig. 4 for the cases in Fig. 3. The C plots considered the conversion on both catalytic surfaces, whereas the G plots were produced by integrating the volumetric gaseous reaction rates over the 7-mm channel height. The predicted homogeneous ignition locations in Fig. 2 closely corresponded to the sharp rise of  $G_{\text{H}_2}$  in Fig. 4 and the  $G_{\text{CO}}$  conversion commenced just downstream of  $G_{\text{H}_2}$  since the gaseous combustion of CO required OH produced by the  $\text{H}_2$  gaseous combustion.

The good agreement between predicted and measured  $x_{ig}$  (or the agreement in the absence of appreciable gaseous combustion above 4 bar) in Fig. 2 could not automatically ensure the validity of the gaseous mechanism, since infinite combinations of catalytic and gas-phase reactivities could produce the same  $x_{ig}$  [38]. Capturing the catalytic processes over the gaseous induction zone

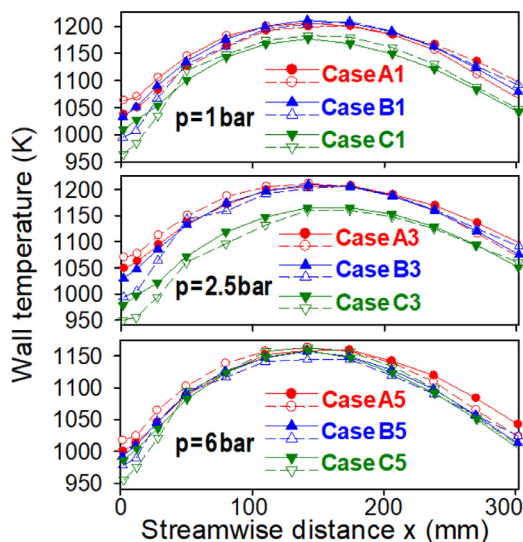


Fig. 3. Upper-wall (filled symbols) and lower-wall (open symbols) temperature measurements for 9 selected cases in Table 1.

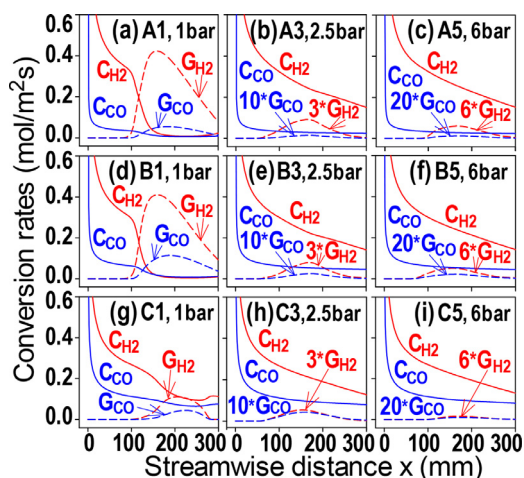


Fig. 4. Computed streamwise profiles of catalytic (C, solid lines) and gas-phase (G, dashed lines) conversion rates of  $H_2$  and CO for the cases in Fig. 3.

$x < x_{ig}$  was imperative to avoid falsification of the gaseous kinetics. To this goal, comparisons between Raman-measured and predicted transverse profiles of  $H_2$ /CO mole fractions are illustrated in Fig. 5 for Cases A4 and C3, at three axial positions  $x < x_{ig}$ . The catalytic conversion was transport-limited for both CO and  $H_2$ , as manifested by the predicted nearly zero mole fractions at the walls ( $y = 0$  and  $7$  mm). The Raman measurements confirmed this behavior, notwithstanding the absence of data closer than  $\sim 0.5$  mm from both walls. While earlier studies at modest  $T_{wall} = 400$ – $800$  K showed

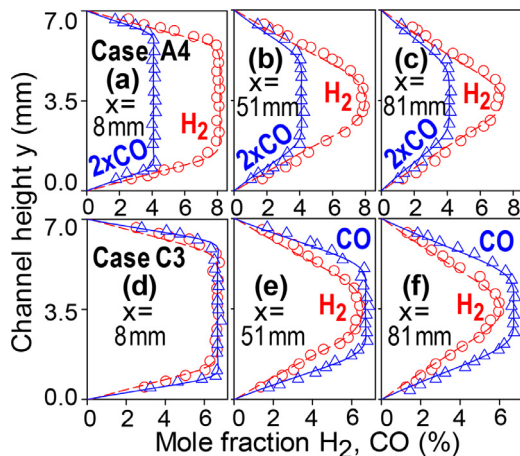


Fig. 5. Predicted (lines) and measured (symbols) transverse profiles of  $H_2$  (circles, dashed-lines) and CO (triangles, solid-lines) for Cases A4 (a-c) and C3 (d-f) at three streamwise positions.

a strong  $H_2$ -CO kinetic coupling over PdO that controlled the light-off of both species [14], the present high  $T_{wall}$  eliminated strong chemical interactions and allowed for fully-ignited (transport-limited) catalytic conversions of both  $H_2$  and CO already from the start of the catalyst.

The gaseous conversion rates  $G$  in Fig. 4 diminished strongly with increasing pressure and mildly with decreasing  $H_2$ :CO volumetric ratios. Gaseous combustion was weak above 2.5 bar, such that for clarity the corresponding  $G$  profiles have been multiplied by factors of 3–20. The dwindling  $G$  conversions with increasing pressure was an outcome of the intrinsic gaseous  $H_2$ /CO kinetics and of the hetero-/homogeneous pathway coupling. The latter resulted predominantly from the strong (transport-limited) catalytic  $H_2$ /CO conversion over  $x < x_{ig}$  that deprived  $H_2$ /CO from the gaseous pathway, while secondary effects included the catalytically-produced  $H_2O$  and the radical adsorption/desorption reactions [33,39].

To clarify the strong pressure dependence in Figs. 2 and 4, the gas-phase ignition characteristics (without including heterogeneous chemistry) of  $\varphi = 0.285$   $H_2$ /CO/air mixtures were studied by calculating the gaseous ignition delay times ( $\tau_{ig}$ ) in a constant-pressure batch reactor using the SENKIN code of CHEMKIN [40]. Computed  $\tau_{ig}$  (determined as the inflection points in the temperature-time histories) versus pressure, with parameter the initial temperature, are plotted in Fig. 6. The initial batch reactor temperature mimicked, for the channel reactor of Fig. 1, a weighted-average between the wall and inlet temperatures (with a larger weight towards the former). The complex behavior in Fig. 6 reflected the second/third explosion limits of  $H_2$  and was a consequence

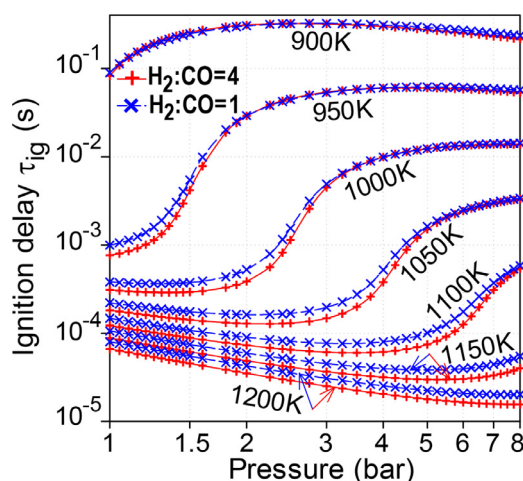


Fig. 6. Computed ignition delays of  $\phi = 0.285$   $\text{H}_2/\text{CO}/\text{air}$  mixtures with  $\text{H}_2:\text{CO}$  volumetric ratios of 4 and 1, at various pressures and initial temperatures.

of the competition between the chain-branching and chain-terminating reactions  $\text{H} + \text{O}_2 \leftrightarrow \text{O} + \text{OH}$  and  $\text{H} + \text{O}_2 + \text{M} \leftrightarrow \text{HO}_2 + \text{M}$ , respectively, and of the branching sequence  $\text{HO}_2 + \text{H}_2 \leftrightarrow \text{H}_2\text{O}_2 + \text{H}$  and  $\text{H}_2\text{O}_2 + \text{M} \leftrightarrow 2\text{OH} + \text{M}$  that became significant at elevated temperatures [41].

Initial temperatures 1000–1100 K in Fig. 6 led to harder gas-phase ignition (longer ignition delays) for  $4 \leq p \leq 8$  bar and could readily explain the homogeneous combustion processes in Fig. 2. Over the extended gas-phase ignition delays at  $p \geq 4$ , the heterogeneous pathway could effectively compete with the gaseous pathway for  $\text{H}_2/\text{CO}$  consumption, thus suppressing homogeneous combustion; this competition was further accentuated by the fast (transport-limited) catalytic consumption shown in Fig. 5. This pressure dependence was evident in Fig. 4 by the dwindling  $G$  conversions with increasing pressure for a given  $\text{H}_2:\text{CO}$  ratio. On the other hand, the weakening  $G$  conversions with decreasing  $\text{H}_2:\text{CO}$  volumetric ratio were a result of the extended ignition delays (compare  $\text{H}_2:\text{CO} = 4$  and 1 in Fig. 6) and also of the generally lower attained  $T_{\text{wall}}$  at lower  $\text{H}_2:\text{CO}$  ratios (see Fig. 3).

#### 4.2. Homogeneous ignition regimes

Of fundamental importance is the delineation of the operating conditions leading to appreciable gas-phase combustion. The “self-regulating” temperature effect [19] (due to the decomposition of  $\text{PdO}$  to  $\text{Pd}$ ) restrains palladium catalysts from achieving the high  $T_{\text{wall}}$  typically needed to ignite homogeneous combustion of hydrocarbons. For example, in  $\text{CH}_4$  combustion over platinum [20]  $T_{\text{wall}}$  up to 1400 K was obtained that facilitated

flame formation, whereas in corresponding studies over palladium [23] the maximum attained  $T_{\text{wall}}$  of 1100 K was insufficient for  $\text{CH}_4$  gaseous ignition. Temperatures up to 1500 K have been obtained in fundamental  $\text{CH}_4$  kinetic studies over palladium, however, by placing the reactor in a temperature-controlled furnace [29]. The present studies were performed at a net heat loss, because the front water-cooling (Fig. 1) was more drastic than the mild rear heating, as discussed in Section 4.  $\text{H}_2/\text{CO}$  fuels with the compositions of Table 1 typically have lower ignition temperatures than hydrocarbons, allowing for appreciable gaseous combustion under nearly-adiabatic or net heat-loss operation. In this respect, the flames in Fig. 2 are the first demonstrated homogeneous combustion results over palladium catalysts.

To delineate regimes of gaseous combustion, simulations were performed in the channel of Fig. 1 for  $\phi = 0.285$  (which is the same  $\phi$  as in the experiments of Fig. 2),  $\text{H}_2:\text{CO} = 1$ , constant  $T_{\text{wall}}$ , inlet temperatures  $T_{\text{IN}} = 300$  K and 650 K,  $U_{\text{IN},0} = 5$  m/s at  $p_0 = 1$  bar and  $U_{\text{IN}} = U_{\text{IN},0} \times (p_0/p)$  at higher pressures so as to maintain the same mass throughput. Isocontours, for which the gaseous ( $G$ ) conversion (summed over  $\text{H}_2$  and  $\text{CO}$ ) comprised a given percentage of the corresponding total gas and catalytic ( $G + C$ ) conversion, were determined by incrementally varying  $T_{\text{wall}}$ . The accessible range of  $T_{\text{wall}}$  in practical systems was limited by the  $\text{PdO}$  decomposition temperatures—in the absence of strong external heating.  $T_{\text{d,low}}$  referred to the lowest temperature for which  $\text{PdO}$  decomposition commenced [17,18] and  $T_{\text{d,high}}$  to an extended temperature limit where  $\text{PdO}$  decomposition was completed ( $\sim 100$  K above  $T_{\text{d,low}}$  [16]). In the tests of Fig. 2 and over the gas-phase induction zones ( $x < x_{\text{ig}}$ ),  $T_{\text{wall}}$  was up to 1196 K such that in some cases  $T_{\text{d,low}} < T_{\text{wall}} < T_{\text{d,high}}$ . Despite the uncertainty on the precise decomposition boundaries, the catalyst could comprise mixed  $\text{PdO}/\text{Pd}$  phases. The simulations, however, captured the Raman-measured transport-limited conversion of both  $\text{H}_2$  and  $\text{CO}$ , suggesting that a potential loss of  $\text{PdO}$  sites to  $\text{Pd}$  when approaching  $T_{\text{d,high}}$  was compensated by a higher reactivity due to the increasing temperature.

The shaded areas in Fig. 7 demarcated regions where gas-phase combustion was appreciable ( $G/(C + G) > 2\%$ ) and was bounded from above by the minimum of the  $T_{\text{d,high}}$  and the adiabatic equilibrium temperature  $T_{\text{ad}}$ . The  $T_{\text{ad}}$  was a conservative limit, as it did not account for the  $\text{H}_2$ -induced surface superadiabaticity. For  $T_{\text{IN}} = 300$  K, gas-phase combustion was modest as it did not account for more than 20% of the total fuel conversion. However, for the gas-turbine-relevant  $T_{\text{IN}} = 650$  K in Fig. 7b, the contribution of gaseous combustion could be substantial, up to 95%. Similar simulations for  $\text{H}_2:\text{CO} = 4$  and  $T_{\text{IN}} = 650$  K



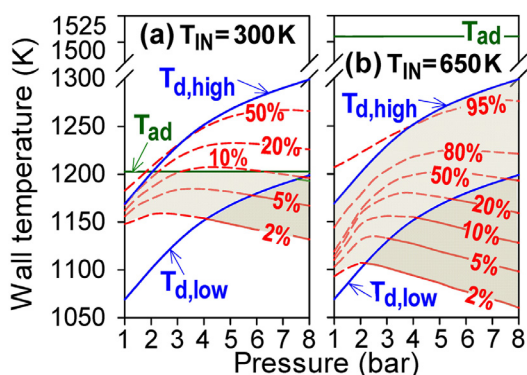


Fig. 7. Computed domains of appreciable gaseous combustion (shaded areas) for  $\text{H}_2/\text{CO}/\text{air}$  ( $\varphi = 0.285$ ,  $\text{H}_2:\text{CO} = 1$ ), (a)  $T_{\text{IN}} = 300\text{ K}$ , (b)  $T_{\text{IN}} = 650\text{ K}$ . Isocontours of constant  $\%G/(C+G)$  conversions are shown.  $T_{\text{d,low}}$  and  $T_{\text{d,high}}$  denote the low and high temperature limits for PdO decomposition and  $T_{\text{ad}}$  the adiabatic equilibrium temperatures.

indicated only minor differences compared to Fig. 7b. Therefore, gas-phase combustion should always be considered during reactor design of syngas-fueled power systems with palladium catalysts.

## 5. Conclusions

The hetero-/homogeneous combustion of fuel-lean  $\text{H}_2/\text{CO}/\text{O}_2/\text{N}_2$  mixtures ( $\varphi = 0.285$ ,  $\text{H}_2:\text{CO}$  volumetric ratios 1-4) over palladium was investigated at pressures 1-8 bar and surface temperatures 950-1200 K, using non-intrusive laser-based measurements and 2-D simulations with detailed chemistry. Raman-measured and predicted transverse profiles of the major species mole fractions attested to a transport-limited catalytic conversion of both  $\text{H}_2$  and CO. XPS measurements after the combustion tests indicated that PdO was the dominant phase on the catalyst surfaces.

PLIF measurements and simulated distributions of the OH radical confirmed the presence of appreciable homogeneous combustion for  $p < 4$  bar which progressively diminished at higher pressures, establishing an agreement between measured and predicted homogeneous ignition distances better than 10.2%. The strong pressure dependence of homogeneous combustion was a result of the competition between catalytic and gaseous pathways for  $\text{H}_2/\text{CO}$  consumption over the gaseous induction zone and of the intricate pressure/temperature dependencies of the gaseous ignition (which was controlled by the  $\text{H}_2$  chemistry).

Over the pre-ignition zones, surface temperatures remained below the extended PdO decomposition limit at each pressure. Despite the self-regulating temperature effect of palladium,

the attained temperatures were sufficient to ignite and sustain homogeneous combustion of syngas mixtures, contrary to hydrocarbons for which gas-phase combustion was largely suppressed. Delineation of the regimes of appreciable homogeneous combustion indicated that gas-phase chemistry could not be ignored for the elevated pressures and preheats of power generation systems.

## Declaration of Competing Interest

None.

## Acknowledgements

Support was provided by SNSF project 200021\_179019. We thank Mr. J. Theile for help in the tests and Dr. M. El Kazzi for the XPS measurements.

## Supplementary materials

Supplementary material associated with this article can be found, in the online version, at doi:10.1016/j.proci.2020.06.262.

## References

- [1] C. Descamps, C. Bouallou, M. Kanniche, *Energy* 33 (2008) 874–881.
- [2] L.O. Nord, R. Anantharaman, O. Bolland, *Int. J. Greenh. Gas Con.* 3 (2009) 385–392.
- [3] N.S. Kaisare, D.G. Vlachos, *Prog. Energy Combust. Sci.* 38 (2012) 321–359.
- [4] R. Sui, E.T. Es-sebbar, J. Mantzaras, N.I. Prasianakis, *Combust. Sci. Technol.* 190 (2018) 336–362.
- [5] Y. Ghermay, J. Mantzaras, R. Bombach, *Proc. Combust. Inst.* 33 (2011) 1827–1835.
- [6] J. Mantzaras, *Combust. Sci. Technol.* 180 (2008) 1137–1168.
- [7] L.L. Smith, H. Karim, M.J. Castaldi, S. Etemad, W.C. Pfefferle, *Catal. Today* 117 (2006) 438–446.
- [8] J. Mantzaras, P. Benz, *Combust. Flame* 119 (1999) 455–472.
- [9] A. Schlegel, S. Buser, P. Benz, H. Bockhorn, F. Mauss, *Symposium (Int.) on Combustion* 25 (1994) 1019–1026.
- [10] J.A. Federici, D.G. Vlachos, *Combust. Flame* 158 (2011) 2540–2543.
- [11] C. Stewart, E.K. Gibson, K. Morgan, G. Cibin, A.J. Dent, C. Hardacre, E.V. Kondratenko, V.A. Kondratenko, C. McManus, S. Rogers, C.E. Stere, S. Chansai, Y.C. Wang, S.J. Haigh, P.P. Wells, A. Goguet, *ACS Catal.* 8 (2018) 8255–8262.
- [12] X. Zheng, J. Mantzaras, R. Bombach, *Combust. Flame* 161 (2014) 332–346.
- [13] R. Sui, J. Mantzaras, R. Bombach, *Combust. Flame* 202 (2019) 292–302.



- [14] R. Sui, W. Liang, L. Zhang, J. Mantzaras, C.K. Law, *Combust. Flame* 211 (2020) 270–280.
- [15] J.G. McCarty, *Catal. Today* 26 (1995) 283–293.
- [16] X.Y. Chen, J.W. Schwank, G.B. Fisher, Y.S. Cheng, M. Jagner, R.W. McCabe, M.B. Katz, G.W. Graham, X.Q. Pan, *Appl. Catal. A: Gen.* 475 (2014) 420–426.
- [17] H. Zhang, J. Gromek, G.W. Fernando, S. Boorse, H.L. Marcus, *J. Phase Equilib.* 23 (2002) 246–248.
- [18] R.A. Dalla Betta, N. Ezawa, K. Tsurumi, J.C. Schlatter, S.G. Nickolas, U.S. Patent No. 5,183,401, 1993.
- [19] T. Griffin, W. Weisenstein, V. Scherer, M. Fowles, *Combust* 101 (1995) 81–90.
- [20] M. Reinke, J. Mantzaras, R. Schaeren, R. Bombach, W. Kreutner, A. Inauen, *Proc. Combust. Inst.* 29 (2002) 1021–1029.
- [21] R. Sui, J. Mantzaras, R. Bombach, A. Denisov, *Proc. Combust. Inst.* 36 (2017) 4321–4328.
- [22] S. Karagiannidis, J. Mantzaras, R. Bombach, S. Schenker, K. Boulouchos, *Proc. Combust. Inst.* 32 (2009) 1947–1955.
- [23] R. Sui, J. Mantzaras, E.T. Es-sebbar, R. Bombach, *Proc. Combust. Inst.* 37 (2019) 5465–5472.
- [24] J. Mantzaras, *Prog. Energy Combust. Sci.* 70 (2019) 169–211.
- [25] M. Schultze, J. Mantzaras, F. Grygier, R. Bombach, *Proc. Combust. Inst.* 35 (2015) 2223–2231.
- [26] J.F. Zhou, S. Matera, S. Pfaff, S. Blomberg, E. Lundgren, J. Zetterberg, *Catalysts* 9 (2019) 484.
- [27] Y. Ghermay, J. Mantzaras, R. Bombach, *Combust. Flame* 157 (2010) 1942–1958.
- [28] J. Mantzaras, R. Bombach, R. Schaeren, *Proc. Combust. Inst.* 32 (2009) 1937–1945.
- [29] T. Shimizu, H. Wang, *Proc. Combust. Inst.* 33 (2011) 1859–1866.
- [30] Y.X. Xin, S. Lieb, H. Wang, C.K. Law, *J. Phys. Chem. C* 117 (2013) 19499–19507.
- [31] M.P. Burke, M. Chaos, Y. Ju, F.L. Dryer, S.J. Klippenstein, *Int. J. Chem. Kinet.* 44 (2012) 444–474.
- [32] J. Li, Z.W. Zhao, A. Kazakov, M. Chaos, F.L. Dryer, J.J. Scire, *Int. J. Chem. Kinet.* 39 (2007) 109–136.
- [33] X. Zheng, J. Mantzaras, R. Bombach, *Combust. Flame* 160 (2013) 155–169.
- [34] M.E. Coltrin, R.J. Kee, F.M. Rupley, *Surface Chemkin, A Fortran Package for Analyzing Heterogeneous Chemical Kinetics at the Solid Surface-Gas Phase Interface*, Sandia National Laboratories, 1996 Report No. SAND90-8003C.
- [35] R.J. Kee, F.M. Rupley, J.A. Miller, I.I. Chemkin, *A Fortran chemical kinetics package for the analysis of gas-phase chemical kinetics*, Sandia National Laboratories, 1996 Report No. SAND89-8009B.
- [36] R.J. Kee, G. Dixon-Lewis, J. Warnatz, M.E. Coltrin, J.A. Miller, *A Fortran Computer Code Package for the Evaluation of Gas-Phase Multicomponent Transport Properties*, Sandia National Laboratories, 1996 Report No. SAND86-8246.
- [37] C. Appel, J. Mantzaras, R. Schaeren, R. Bombach, A. Inauen, *Combust. Flame* 140 (2005) 70–92.
- [38] J. Mantzaras, C. Appel, *Combust. Flame* 130 (2002) 336–351.
- [39] Y. Ghermay, J. Mantzaras, R. Bombach, K. Boulouchos, *Combust. Flame* 158 (2011) 1491–1506.
- [40] A.E. Lutz, R.J. Kee, J.A. Miller, *SENKIN: A Fortran Program for Predicting Homogeneous Gas Phase Chemical Kinetics with Sensitivity Analysis*, Sandia National Laboratories, 1996 Report No. SAND87-8248.
- [41] I. Glassman, *Combustion*, 3rd Ed., Academic Press, London, 1996.